

# The response of the coupled magnetosphere-ionosphere-thermosphere system to a 25% reduction in the dipole moment of the Earth's magnetic field

Ingrid Cnossen,<sup>1</sup> Arthur D. Richmond,<sup>1</sup> Michael Wiltberger,<sup>1</sup> Wenbin Wang,<sup>1</sup> and Peter Schmitt<sup>1</sup>

Received 8 August 2011; revised 7 September 2011; accepted 21 September 2011; published 3 December 2011.

[1] The Earth's magnetic field changes in orientation and strength over time. We study the response of the magnetosphere-ionosphere-thermosphere system to a 25% reduction in magnetic field intensity, using the coupled magnetosphere-ionosphere-thermosphere (CMIT) model. Simulations were performed with a dipole moment of  $8 \times 10^{22}$  A m<sup>2</sup>, close to the present-day value, and a dipole moment of  $6 \times 10^{22}$  A m<sup>2</sup>, both under the same solar wind conditions, intermediate solar activity (F10.7 = 150), and for March equinox and June solstice. The 25% reduction in field strength causes the magnetosphere to shrink and the polar cap to expand, in agreement with theory. The Pedersen and the Hall ionospheric conductances increase by 50%–60% and 60%–65%, respectively. This causes a ~9%–12% decrease in electric potential and a ~20% increase in field-aligned currents during equinox. Ion  $\mathbf{E} \times \mathbf{B}$  drift velocities are enhanced by ~10%–15%. The Joule heating also increases, by 13%–30%, depending on the season. Changes in the neutral temperature structure are caused partly by changes in Joule heating and partly by changes in the neutral wind. The neutral wind itself is also affected by changes in neutral temperature and by changes in ion velocities. The changes in the neutral wind, together with changes in the vertical component of the  $\mathbf{E} \times \mathbf{B}$  drift, affect the height of the ionospheric F2 layer. Changes in electron density are related to changes in the O/N<sub>2</sub> ratio. The global mean increase in neutral temperature causes the thermosphere to expand, resulting in a global mean uplift of the ionosphere. These effects are generally smaller during solstice.

**Citation:** Cnossen, I., A. D. Richmond, M. Wiltberger, W. Wang, and P. Schmitt (2011), The response of the coupled magnetosphere-ionosphere-thermosphere system to a 25% reduction in the dipole moment of the Earth's magnetic field *J. Geophys. Res.*, 116, A12304, doi:10.1029/2011JA017063.

## 1. Introduction

[2] The Earth's magnetic field varies slowly in strength and in orientation, and also the relative contributions of the main dipole component and higher-order field components vary. We are currently at a time of a relatively strong change in terms of field intensity, as the Earth's dipole moment has decreased by about 5% per century since 1840, while little change in field strength occurred from 1590 to 1840 [Gubbins *et al.*, 2006]. Between 1910 and 2010 the change in dipole moment according to the International Geomagnetic Reference Field (IGRF) [Finlay *et al.*, 2010] was even 6.3%. Still, changes as are occurring at present are not uncommon in the geological record. Guyodo and Valet [1999] show that the Earth's dipole moment has been varying on average between  $\sim 4 \times 10^{22}$  A m<sup>2</sup> and  $\sim 9 \times 10^{22}$  A m<sup>2</sup> over the past 800,000 years, with occasionally values still

more extreme than that. The current dipole moment is  $\sim 7.7 \times 10^{22}$  A m<sup>2</sup>, and thus still relatively high, despite the decrease that has taken place over the past 170 years.

[3] Long-term changes in the Earth's magnetic field are theoretically expected to cause changes in the magnetosphere and ionosphere, with potential consequences also for the thermosphere, the neutral part of the upper atmosphere. So far, effects on the magnetosphere and the upper atmosphere have been estimated separately, through theoretical work and a few modeling studies.

[4] Siscoe and Chen [1975] and Glassmeier *et al.* [2004] derived scaling relations for magnetospheric parameters with the dipole moment  $M$ . From the pressure balance at the magnetopause between the solar wind dynamic pressure and the magnetic pressure from the Earth's magnetic field, it can be found that the standoff distance  $R_s$  scales as  $R_s \propto M^{1/3}$  [e.g., Kivelson and Russell, 1995]. From this first scaling relation, others were derived based on the main assumption of "self-similarity," i.e., no change in the shape of the magnetosphere.

[5] Zieger *et al.* [2006a, 2006b] subsequently used the analytical Hill-Siscoe model [Hill *et al.*, 1976; Siscoe *et al.*,

<sup>1</sup>High Altitude Observatory, National Center for Atmospheric Research, Boulder, Colorado, USA.

2002a, 2002b] and the BATS-R-US magnetohydrodynamic (MHD) model to verify the theoretical scaling relations derived by the studies mentioned above. They suggested some modifications, mainly a dependence of the scaling with  $M$  on the  $B_z$  component of the interplanetary magnetic field (IMF), but they did not find any significant deviation from self-similarity. A weakness in their approach was that their model did not include the ionosphere, and instead assumed a constant, uniform conductance as the inner boundary condition for the magnetospheric simulations. This conductance was manually adjusted for each simulation according to  $\Sigma_P \propto M^{-1}$ , following the work of *Glassmeier et al.* [2004].

[6] Independently from the above studies, *Cnossen and Richmond* [2008] investigated the effect of changes in the Earth's magnetic field on the ionosphere. However, instead of investigating changes in dipole moment only, they performed simulations with the full magnetic fields of 1957 and 1997 using the thermosphere-ionosphere-electrodynamics general circulation model (TIE-GCM). They found that changes that had occurred between 1957 and 1997 had a substantial effect on the ionosphere in certain regions where magnetic field changes had been relatively large (mainly over South America and the southern Atlantic Ocean), while being negligible in other parts of the world. However, since their model did not include the magnetosphere, they could not assess the effects of changes in the high-latitude coupling between the magnetosphere and ionosphere-thermosphere system, which could be important.

[7] In this study, we aim to investigate the effect of changes in the dipole moment of the Earth's magnetic field on the coupled system consisting of the magnetosphere, ionosphere, and thermosphere, rather than studying the individual components in isolation, which may not give the correct answer. This is a first step in quantifying, and getting to understand, how the magnetosphere-ionosphere-thermosphere system responds to a change in the geomagnetic field. In a future study we will do a similar analysis for changes in dipole orientation. The results from that study and the present one will be the stepping stones to help us interpret the responses to changes in the magnetic field of the Earth that have occurred historically. This is necessary to understand better how long-term trends in the upper atmosphere have formed, and it may also improve our knowledge of the coupling between the magnetosphere, ionosphere, and thermosphere in general.

[8] This paper is organized as follows. In section 2 we describe the model that was used and the settings used specifically for the simulations in our study. In section 3 we present the results, starting from the magnetosphere, and working inward toward the high-latitude ionosphere and thermosphere, finishing with global responses in the ionosphere-thermosphere system. This is followed by a discussion of the results in section 4, and a summary and conclusions in section 5.

## 2. Methodology

### 2.1. Model Description

[9] We investigate the effects of a 25% reduction in magnetic field strength using the coupled magnetosphere-ionosphere-thermosphere (CMIT) model [*Wiltberger et al.*,

2004; *Wang et al.*, 2004; *Wang et al.*, 2008]. The CMIT model couples the Lyon-Fedder-Mobarry (LFM) global magnetospheric code [*Lyon et al.*, 2004] with the thermosphere-ionosphere-electrodynamics general circulation model (TIE-GCM) [*Roble et al.*, 1988; *Richmond et al.*, 1992].

[10] The LFM code solves the ideal magnetohydrodynamic (MHD) equations to simulate the interaction between the solar wind and the magnetosphere. It calculates the full MHD state vector (plasma density, pressure, velocity, and magnetic field) on a distorted spherical grid. It requires the solar wind MHD state vector on its outer boundary as input and uses an empirical parameterization [*Wiltberger et al.*, 2009] to calculate the energy flux of precipitating electrons. On its inner boundary it requires the ionospheric conductance to calculate the electric potential. In CMIT it receives this from the TIE-GCM part of the code.

[11] The TIE-GCM is a time-dependent, three-dimensional model that solves the fully coupled, nonlinear, hydrodynamic, thermodynamic, and continuity equations of the thermospheric neutral gas self-consistently with the ion continuity equations. In the stand-alone version, auroral particle precipitation from the magnetosphere is parameterized through specifying the hemispheric power, and the high-latitude electric field is externally imposed using the *Heelis et al.* [1982] or *Weimer* [1995, 2005] model. In CMIT, these quantities are fed into TIE-GCM from the LFM part of the code. The coupling of the LFM and TIE-GCM in CMIT thus enables the calculation of the global ionospheric electric field, which includes both the imposed high-latitude electric field from the magnetosphere and the dynamo electric fields generated by thermospheric winds. This makes it possible to study the dynamical coupling between the magnetosphere and the ionosphere-thermosphere system.

### 2.2. Simulation Setup and Analysis

[12] For our simulations we have simplified the specification of the Earth's internal magnetic field to a centered dipole, instead of using the IGRF [*Finlay et al.*, 2010], which is normally used. For one set of simulations, the strength of this dipole was set to  $8.00 \times 10^{22}$  A m<sup>2</sup>, close to the present-day value, while for the second set of simulations it was set to  $6.00 \times 10^{22}$  A m<sup>2</sup>. These simulation sets will be referred to as "strong dipole" and "weak dipole," respectively. The position of the northern hemisphere (NH) geomagnetic pole was kept fixed at 80°N and 70°W for all simulations.

[13] Simulations with a duration of 36 h were performed for the March equinox and the June solstice, both under moderate solar activity conditions ( $F_{10.7} = 150$ ) and starting at 0 UT. Idealized solar wind conditions were used. The solar wind density was set to a constant value of  $5 \text{ cm}^{-3}$ , and the outward solar wind speed was set to 400 km/s, while the speed in the GSM  $y$  and  $z$  directions was set to zero. The  $B_z$  component of the IMF was set to  $-5$  nT for the first two hours (0–2 UT),  $+5$  nT for the second two hours (2–4 UT), and  $-5$  nT for the rest of the simulation, while the  $B_x$  and  $B_y$  components were set to zero for the full duration of the simulations. The IMF components are defined in GSM coordinates. The sound speed of the plasma in the solar wind was set to a constant 40 km/s, ensuring that the incoming solar wind was highly supersonic.

**Table 1.** Standoff Distance for the Strong and Weak Dipole: Mean and Standard Deviation Over the Last 24 h of the Simulations

Dipole	Standoff Distance ( $R_E$ )			
	March Equinox		June Solstice	
	Mean	$\sigma$	Mean	$\sigma$
Strong dipole	9.9	0.1	10.3	0.2
Weak dipole	8.8	0.1	9.2	0.3

[14] These settings bring the modeled magnetosphere into a quasi-steady state soon after 4 UT. After 4 UT no substorms are present in the simulations, and we thus study the magnetosphere-ionosphere-thermosphere system under steady conditions, although the magnetospheric driving is relatively strong. Any differences between the strong and weak dipole simulations that might arise in terms of the frequency and intensity of substorms are not considered here.

[15] The ionosphere-thermosphere system needs more time than the magnetosphere to reach a quasi-steady state. From the time series of the mean exospheric temperature we find that this takes about 12 h. We therefore consider only the last 24 h of our simulations, or a subinterval within that period, to compare the weak and strong dipole simulations and characterize the differences between them.

[16] We focus primarily on the average differences between the strong and weak dipoles and present most results in the form of a mean with standard deviation over the last 24 h of the simulations. Data are output every 6 min, so that this gives an average over 240 values. To show the spatial structure of differences in variables, we also present maps for the interval of 13–15 UT. A 2 h window was chosen to average out short-term variations, while not smoothing features dependent on local time too much. The 13–15 UT interval was chosen because it gives a fair representation of the overall differences between the strong and weak dipole simulations in all the variables we study. However, background fields as well as difference fields do vary over time. Any substantial differences with other time frames are commented on briefly in the text, but are not studied in detail.

### 3. Results

#### 3.1. Size and Shape of the Magnetosphere

[17] As the geomagnetic field intensity decreases, the magnetosphere is expected to contract. The most basic parameter to characterize the size of the magnetosphere is the distance from the center of the Earth to the magnetopause in the  $x$  direction (toward the Sun), also called the standoff distance. Table 1 presents the average standoff distance and the standard deviation for the strong and weak dipoles over the last 24 h of the simulations. This was calculated in GSM coordinates, resulting in a slightly larger standoff distance during solstice that is due to the larger tilt of the dipole with respect to the GSM  $x$  direction in this season.

[18] For both equinox and solstice, the standoff distance is 1.1  $R_E$  smaller for the weak dipole than for the strong dipole. Because the mean standoff distance is larger for solstice than for equinox, this means that the ratio of the strong and weak dipole standoff distance is slightly larger under equinox conditions. If the magnetosphere is assumed to be self-

similar, i.e., not changing in shape, the ratio between the standoff distance for the strong and weak dipoles can be used to scale other magnetospheric distances as well. Figure 1 shows the shape of the magnetosphere for the weak and strong dipoles in the  $x$ - $y$  plane at  $z = 0$  (in solar magnetic coordinates) at 14 UT (during IMF southward conditions) for equinox, determined from the position where  $B_z = 0$ . This works in our case because  $B_z < 0$  in the solar wind for the entire time interval we study, while  $B_z > 0$  in the magnetosphere at  $z = 0$ . There is no noticeable difference in magnetosphere shape between the two simulations, except in the tail, where the boundary is less well defined (not shown). Although the overall shape of the magnetosphere varies with time, and between solstice and equinox conditions, we find that it does generally remain similar for the weak and strong dipoles. The assumption of self-similarity therefore appears to be a reasonable one.

#### 3.2. Polar Cap

[19] A consequence of the reduction in magnetic field strength and the size of the magnetosphere is that the last closed field lines map to lower geomagnetic latitudes, increasing the size of the polar cap. The average northern hemisphere (NH) polar cap area (defined as the area enclosed by the open or closed field line boundary) and the average NH latitude of the polar cap boundary for the weak

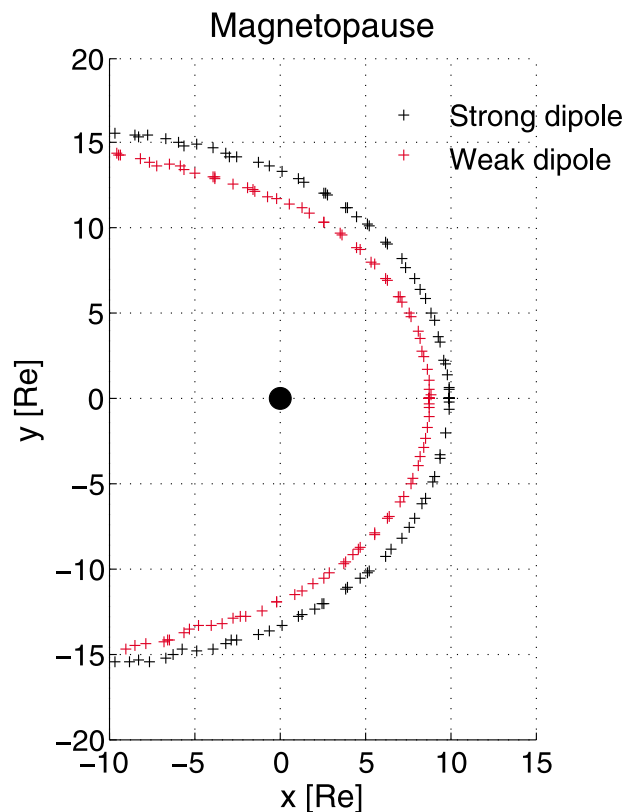


**Figure 1.** Size and shape of the magnetosphere viewed in the solar-magnetic  $x$ - $y$  plane ( $z = 0$ ) for the strong dipole (black) and the weak dipole (red) for equinox at 14 UT. The boundary is defined as  $B_z = 0$ , which marks the crossing from the Earth's magnetic field, for which  $B_z > 0$ , to the IMF, for which  $B_z < 0$  at 14 UT.

**Table 2.** NH Polar Cap Area and Polar Cap Geomagnetic Latitude for the Strong and Weak Dipole: Mean and Standard Deviation Over the Last 24 h of the Simulations

Dipole	NH Polar Cap Area ( $10^6$ km $^2$ )				NH Polar Cap Geomagnetic Latitude ( $^{\circ}$ N)			
	March Equinox		June Solstice		March Equinox		June Solstice	
	Mean	$\sigma$	Mean	$\sigma$	Mean	$\sigma$	Mean	$\sigma$
Strong dipole	7.3	0.3	7.3	0.3	76.3	0.3	76.3	0.3
Weak dipole	8.1	0.3	8.3	0.5	75.6	0.3	75.3	0.4

and strong dipoles are given in Table 2. The NH latitude of the polar cap boundary was calculated based on the polar cap area, assuming a circular polar cap. This gives a measure of the average position of the polar cap boundary. The polar cap area increased by  $\sim 11\%$ – $14\%$ , while the geomagnetic latitude of the polar cap boundary decreased by  $\sim 1^{\circ}$  for both equinox and solstice. The percentage difference quoted above is based on the ratio of weak dipole to strong dipole. This will also be the case for any percentages quoted in the following sections, unless stated otherwise in the text.

### 3.3. Ionospheric Conductivity

[20] The ionospheric Pedersen and Hall conductivities are calculated as follows [e.g., *Richmond, 1995*]:

$$\sigma_P = \frac{N_e e}{B} \left( \frac{\nu_{in} \Omega_i}{\nu_{in}^2 + \Omega_i^2} + \frac{\nu_{en\perp} \Omega_e}{\nu_{en\perp}^2 + \Omega_e^2} \right), \quad (1a)$$

$$\sigma_H = \frac{N_e e}{B} \left( \frac{\Omega_e^2}{\nu_{en\perp}^2 + \Omega_e^2} - \frac{\Omega_i^2}{\nu_{in}^2 + \Omega_i^2} \right), \quad (1b)$$

where  $\sigma_P$  is the Pedersen conductivity,  $\sigma_H$  is the Hall conductivity,  $N_e$  is the electron number density,  $e$  is the magnitude of the electron charge,  $B$  is the magnitude of the magnetic field,  $\nu_{in}$  is the collision frequency of ions with neutrals,  $\nu_{en\perp}$  is the collision frequency of electrons with neutrals in the direction perpendicular to the magnetic field,  $\Omega_i$  is the ion gyrofrequency, and  $\Omega_e$  is the electron gyrofrequency. The ion and electron gyrofrequencies are in turn given by

$$\Omega_i = eB/m_i, \quad (2a)$$

$$\Omega_e = eB/m_e, \quad (2b)$$

where  $m_i$  is the ion mass and  $m_e$  is the electron mass. The magnitude of the Earth's magnetic field  $B$  thus enters the equations for both conductivities directly, as well as by its influence on the ion and electron gyrofrequencies. A strong effect of a change in magnetic field strength on the ionospheric conductivity is therefore expected.

[21] The modeled Hall and Pedersen field-line-integrated conductivity (also called conductance) patterns for the strong dipole simulation, averaged over 13–15 UT and averaged over the northern hemisphere (NH) and southern hemisphere (SH) for equinox, are shown in Figure 2 (left). Figure 2 (right) shows the ratio between the weak and strong

dipole conductance patterns for the same time frame (weak/strong dipole). On the dayside, the Hall conductance is  $\sim 60\%$ – $65\%$  larger and the Pedersen conductance is  $\sim 50\%$ – $60\%$  larger for the weak dipole than for the strong dipole. On the nightside, where the conductances are small, the relative differences are generally also smaller. Still, an enhancement in the Hall conductance along the auroral oval of 20%–40% can be seen. This is not found for the Pedersen conductance for the time frame shown, but similar enhancements on the nightside as seen for the Hall conductance do occur during some other UT intervals. For solstice the absolute differences are somewhat smaller, but because the combined NH and SH conductances are lower during solstice than during equinox, the relative differences between the weak and strong dipole are similar.

[22] Energetic particle precipitation contributes to the ionospheric conductivity, mainly on the nightside. We use the hemispheric power of precipitating particles as a measure of its strength, with mean values and standard deviations over the last 24 h given in Table 3. The particle precipitation power for the weak dipole is mostly larger than for the strong dipole (except for solstice in the SH), but only by a small margin, considering the relatively large standard deviation. We may therefore conclude that there is no significant difference in particle precipitation.

### 3.4. Field-Aligned Currents and Cross-Polar Cap Potential

[23] The ionospheric conductance serves as a boundary condition for the magnetosphere, as magnetospheric current systems close in the high-latitude ionosphere. The ionospheric conductivity affects the amount of current that can flow through the ionosphere as well as the high-latitude electric field potential distribution. This can be readily understood from the following condition, which follows from Ohm's law and current continuity:

$$\nabla_{\perp} \cdot (\Sigma \cdot \nabla_{\perp} \Phi) = J_{\parallel}, \quad (3)$$

where  $\Sigma$  is the ionospheric conductance,  $\Phi$  is the electric field potential, and  $J_{\parallel}$  is the upward field-aligned current. If  $\Sigma$  increases, either  $J_{\parallel}$  must increase also (if the electric field potential distribution is assumed to stay constant) or  $\nabla_{\perp} \Phi (= -\mathbf{E})$  must decrease (if  $J_{\parallel}$  is assumed to stay constant). In practice, something in between these extremes happens, where both  $\nabla_{\perp} \Phi$  and  $J_{\parallel}$  adjust to balance the increase in  $\Sigma$ . This is shown in Figure 3 for the NH during equinox for 13–15 UT. Note that the field-aligned currents are primarily region 1 currents. The model generates only very weak region 2 currents, as has been noted before for the stand-alone LFM [*Korth et al., 2004*]. The changes in the field-aligned currents occur mainly on the dayside, where the largest changes in conductance were also found.

[24] To characterize the changes in the electric field potential and field-aligned current distributions during the last 24 h of the simulations, the mean and standard deviation of the cross-polar cap potential and the total hemispherically integrated current (upward + downward) are given in Tables 4 and 5, respectively. The cross-polar cap potential is on average  $\sim 9\%$ – $12\%$  smaller for the weak dipole, except in the SH for June solstice, when the difference is very small. The field-aligned currents show an increase of  $\sim 20\%$  for

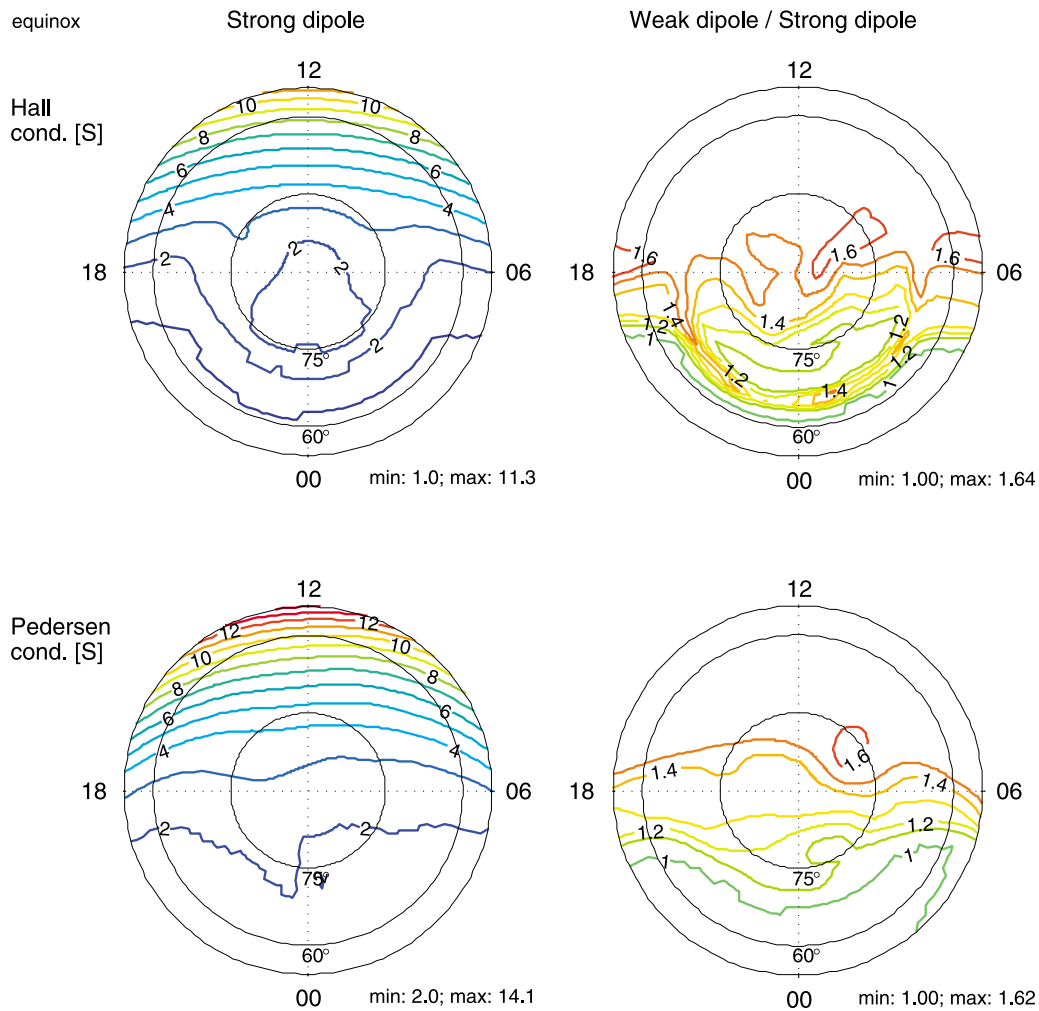


**Figure 2.** The averaged NH and SH (top) Hall and (bottom) Pedersen conductance for (left) the strong dipole and (right) the weak-strong dipole for equinox at 13–15 UT. The view is centered on the dipole, with local noon to the top.

both hemispheres during March equinox and for the NH during June solstice. The SH field-aligned currents do not change significantly for June solstice, which is probably due to a smaller change in ionospheric conductance during winter, associated with a lack of sunlight.

### 3.5. The High-Latitude Ionosphere and Thermosphere

[25] Ion drift velocities are given by  $\mathbf{E} \times \mathbf{B}/B^2$ , so that their magnitude scales as  $E/B$ . The reduction the electric field potential was  $\sim 10\%$ . If we assume that the distance between the potential maximum and minimum scales in the same way as the change in the colatitude of the polar cap boundary, this gives an increase in that distance of a factor  $\sim 14.55/13.7 = 1.06$  (6%). The change in the electric field  $E$  can then be approximated as  $0.9/1.06 = 0.85$ , and we can predict an increase in ion velocities by a factor of  $0.85/0.75 = 1.13$ , so  $\sim 13\%$ . The simulated changes in horizontal ion drift velocities agree quite well with this estimate. They are of the order of  $\sim 10\%$ – $15\%$ , as shown in Figure 4 (top) for the NH under equinox conditions for 13–15 UT. The differences, as well as the ion drifts for the control case (strong dipole), vary considerably over time,

and some other time intervals do show stronger changes. Generally speaking, the changes show an enhancement of the existing  $\mathbf{E} \times \mathbf{B}$  drift pattern, although there can be a small rotation of the pattern as well, which depends on the time interval studied. This is also true at June solstice.

[26] An increase in ion drift velocities can affect the neutral winds through ion-neutral collisions. The efficiency of

**Table 3.** Hemispheric Power of Precipitating Particles in the NH and SH for the Strong Dipole, Weak Dipole, and the Difference: Mean and Standard Deviation Over the Last 24 h of the Simulations

Dipole	NH Power of Precip. Particles (GW)				SH Power of Precip. Particles (GW)			
	March Equinox		June Solstice		March Equinox		June Solstice	
	Mean	$\sigma$	Mean	$\sigma$	Mean	$\sigma$	Mean	$\sigma$
Strong dipole	2.4	0.7	3.0	0.4	2.5	0.7	5.1	0.5
Weak dipole	2.8	0.9	3.2	0.5	2.8	0.9	5.1	0.5
Weak-strong	0.4	0.6	0.2	0.3	0.3	0.5	0.0	0.7

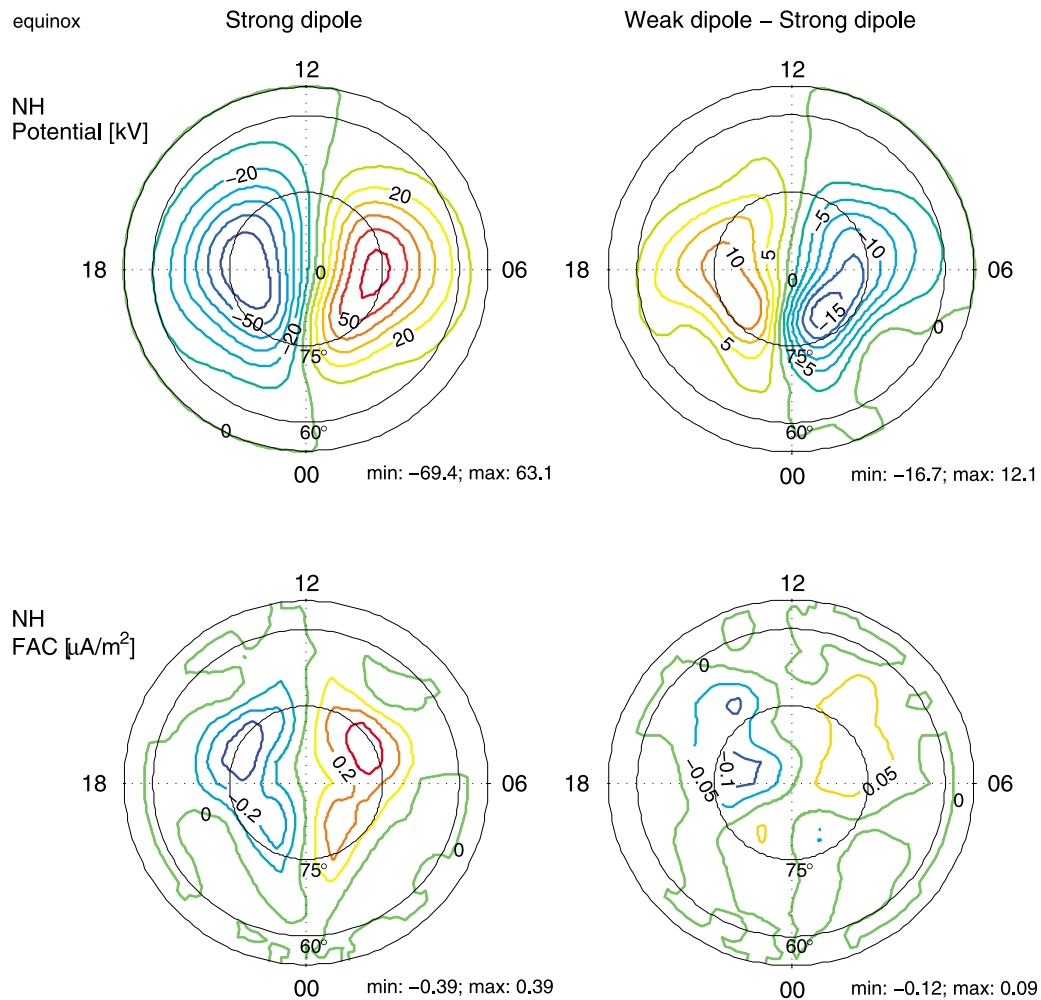


**Figure 3.** The NH (top) electric field potential and (bottom) field-aligned current patterns for (left) the strong dipole and (right) the weak-strong dipole for equinox at 13–15 UT. The view is centered on the dipole, with local noon to the top.

this process depends on the so-called ion drag coefficients, which in the F region are proportional to the electron density, and on the difference between the ion and neutral velocities (see, e.g., *Richmond* [1995] for further details). The neutral wind pattern at high latitudes appears to be enhanced in a similar way to the high-latitude  $\mathbf{E} \times \mathbf{B}$  drifts (Figure 4, bottom). Changes in the neutral winds are also seen at lower latitudes (<65°N), and they tend to be stronger

than the very high latitude changes. In the premidnight sector mainly the meridional neutral wind is enhanced, while in other local time sectors mainly the zonal neutral wind is enhanced. These changes cannot be caused by the changes in the horizontal  $\mathbf{E} \times \mathbf{B}$  drift, as they are smaller at low latitudes than the changes in the neutral winds. We must

**Table 4.** Cross-Polar Cap Potential in the NH and SH for Strong Dipole, Weak Dipole, and the Difference (Weak-Strong Dipole): Mean and Standard Deviation Over the Last 24 h of the Simulations

Dipole	NH Cross-Polar Cap Potential (kV)				SH Cross-Polar Cap Potential (kV)			
	March Equinox		June Solstice		March Equinox		June Solstice	
	Mean	$\sigma$	Mean	$\sigma$	Mean	$\sigma$	Mean	$\sigma$
Strong dipole	130	11	83	18	131	11	93	20
Weak dipole	119	10	74	17	120	10	90	17
Weak-strong	-11	8	-9	6	-10	7	-3	7

**Table 5.** Total Field-Aligned Current in the NH and SH for the Strong Dipole, Weak Dipole, and the Difference (Weak-Strong Dipole): Mean and Standard Deviation Over the Last 24 h of the Simulations<sup>a</sup>

Dipole	NH Field-Aligned Current (10 <sup>6</sup> A)				SH Field-Aligned Current (10 <sup>6</sup> A)			
	March Equinox		June Solstice		March Equinox		June Solstice	
	Mean	$\sigma$	Mean	$\sigma$	Mean	$\sigma$	Mean	$\sigma$
Strong dipole	3.5	0.5	4.2	0.2	3.4	0.4	2.2	0.4
Weak dipole	4.2	0.9	5.1	0.4	4.1	0.9	2.3	0.4
Weak-strong	0.7	0.5	0.9	0.4	0.6	0.5	0.1	0.2

<sup>a</sup>Approximately half of the total current is upward and half of it is downward directed.

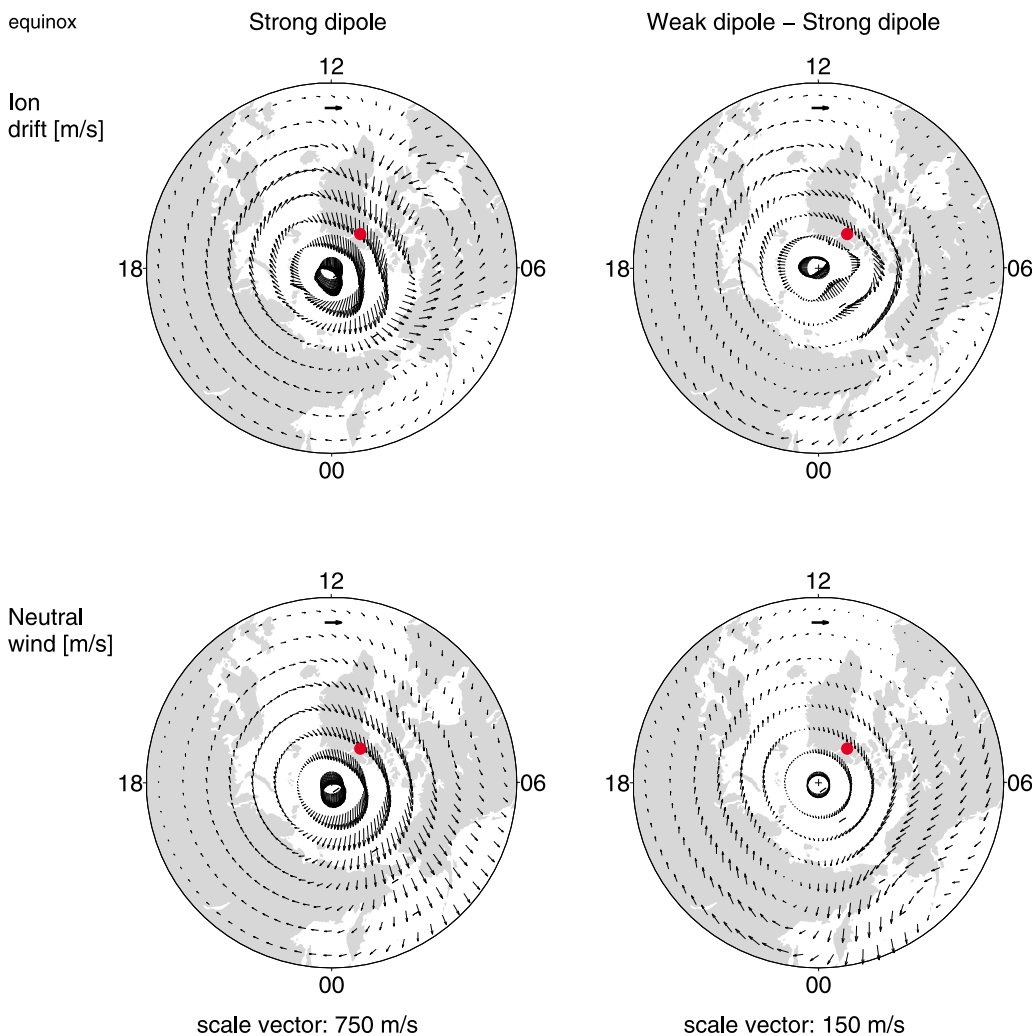


**Figure 4.** The NH (top) horizontal  $\mathbf{E} \times \mathbf{B}$  drift and (bottom) neutral wind at  $3.2 \times 10^{-8}$  hPa ( $\sim 380$  km) for (left) the strong dipole and (right) the weak-strong dipole for equinox at 13–15 UT. The view is centered on the geographic pole, with local noon to the top and the outer boundary at  $50^\circ\text{N}$ . The position of the dipole is marked with a red dot.

therefore consider other factors influencing the neutral wind as well.

[27] One such factor is the pressure gradient, which is linked to the neutral temperature gradient. The neutral temperature in turn is determined by heating and cooling processes. In the high-latitude ionosphere, Joule heating is one of the most important heating mechanisms. It can be calculated as follows:

$$Q_J = \sigma_P B^2 [(U_i - U_n)^2 + (V_i - V_n)^2 + (W_i - W_n)^2], \quad (4)$$

where  $Q_J$  is the Joule heating per unit volume,  $\sigma_P$  is the Pedersen conductivity,  $B$  is the magnetic field strength,  $U_i$ ,  $V_i$ , and  $W_i$  are the zonal, meridional, and vertical ion  $\mathbf{E} \times \mathbf{B}$  drift velocities, respectively, and  $U_n$ ,  $V_n$ , and  $W_n$  are the zonal, meridional, and vertical neutral wind velocities, respectively. Changes in the neutral wind can thus alter the Joule heating, and changes in Joule heating can in turn also alter the neutral winds.

[28] The ion drift velocities and neutral winds were both enhanced as a result of the reduction in  $B$ , but it is not immediately obvious whether the difference between them would have increased or decreased. However, when we calculate  $(U_i - U_n)^2$  and  $(V_i - V_n)^2$  we find that both have mainly increased, while  $(W_i - W_n)^2$  makes only a small

**Table 6.** NH and SH Joule Heating Power for the Strong Dipole, Weak Dipole, and the Difference (Weak-Strong Dipole): Mean and Standard Deviation Over the Last 24 h of the Simulation

Dipole	NH Joule Heating Power (GW)				SH Joule Heating Power (GW)			
	March Equinox		June Solstice		March Equinox		June Solstice	
	Mean	$\sigma$	Mean	$\sigma$	Mean	$\sigma$	Mean	$\sigma$
Strong dipole	59.0	14.0	50.8	12.9	55.8	12.0	20.6	7.1
Weak dipole	75.3	14.0	57.4	17.6	72.6	14.8	26.0	9.4
Weak-strong	16.2	9.0	6.6	8.1	16.8	8.2	5.4	3.7

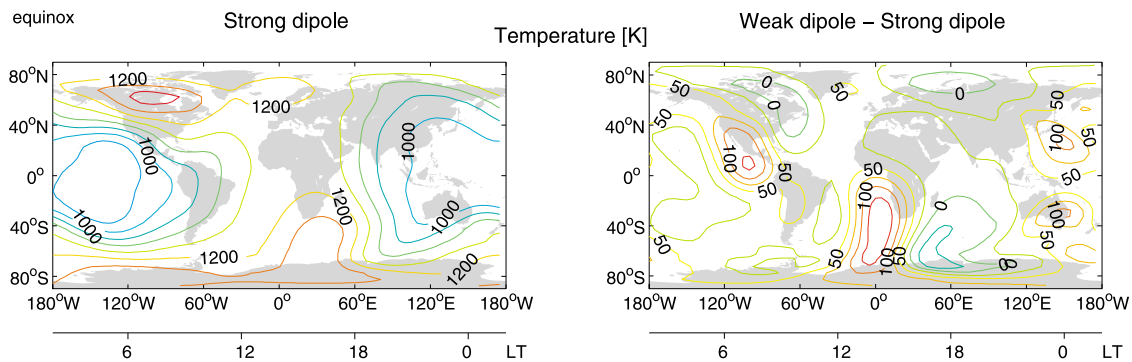


**Figure 5.** The temperature in the thermosphere at  $3.2 \times 10^{-8}$  hPa ( $\sim 380$  km) for (left) the strong dipole and (right) the weak-strong dipole for equinox at 13–15 UT in geographic coordinates.

contribution in any case. Our results indicate that this effect, together with the increase in  $\sigma_P$  above 125 km, outweighs the reduction in  $B^2$ , because we find that the Joule heating has increased for the weak dipole compared with the strong dipole. This is shown in Table 6, which presents the Joule heating power, here defined as the Joule heating integrated hemispherically and in height.

[29] The Joule heating power is consistently larger for the weak dipole than for the strong dipole. The relative difference is smallest (13%) and least significant during June solstice in the NH. In all other cases the Joule heating power is 26%–30% larger for the weak dipole than for the strong dipole.

[30] The changes in Joule heating power occur primarily at high latitudes ( $>60^\circ$ ), although an increase in Joule heating power is found down to  $\sim 30^\circ\text{N}$  over North America for the 13–15 UT time interval studied before (not shown). The increase in high-latitude Joule heating is expected to cause higher temperatures there, leading to a larger meridional temperature gradient, and therefore a larger meridional pressure gradient. This should strengthen the meridional winds, and as the Coriolis force deflects these meridional winds, the zonal winds will also be affected.

### 3.6. The Global Ionosphere and Thermosphere

[31] Figure 5 shows the global temperature structure for the strong dipole and the difference (strong – weak dipole) for equinox at 13–15 UT. The differences in temperature are predominantly positive, but they vary with latitude and

longitude and can even be negative in some regions. The global difference pattern moves with local time and also changes somewhat in exact shape and strength over time.

[32] Despite the relatively large changes in Joule heating, occurring primarily at high latitudes, the largest temperature changes are not found at high latitudes, indicating that other processes are also important. Our results suggest that some of the temperature changes in fact may be caused by changes in the horizontal neutral wind. For instance, the changes in temperature in the southern Atlantic and Indian oceans ( $10^\circ\text{S}–80^\circ\text{S}$ ;  $30^\circ\text{W}–100^\circ\text{E}$ ) seem to be due to a westward shift of the temperature structure for the control case (strong dipole), caused by stronger westward winds. Changes in the neutral wind are thus responsible for changes in temperature in some cases, but the changes in temperature must in turn also affect the neutral winds through changes in pressure gradients. Responses in temperature and neutral wind therefore form together.

[33] While the responses in temperature are clearly not spatially uniform, it can be useful to summarize the changes in the form of a global mean. This is done in Figure 6 (left), which shows the global mean temperature profile for the strong and weak dipoles for both equinox and solstice, averaged over the last 24 h of the simulations. The overall increase in thermospheric temperature is strongest during equinox. A quantitative summary of the changes in exospheric temperature is given in Table 7.

[34] As a result of the increase in temperature, the thermosphere expands, and ionospheric layers should move

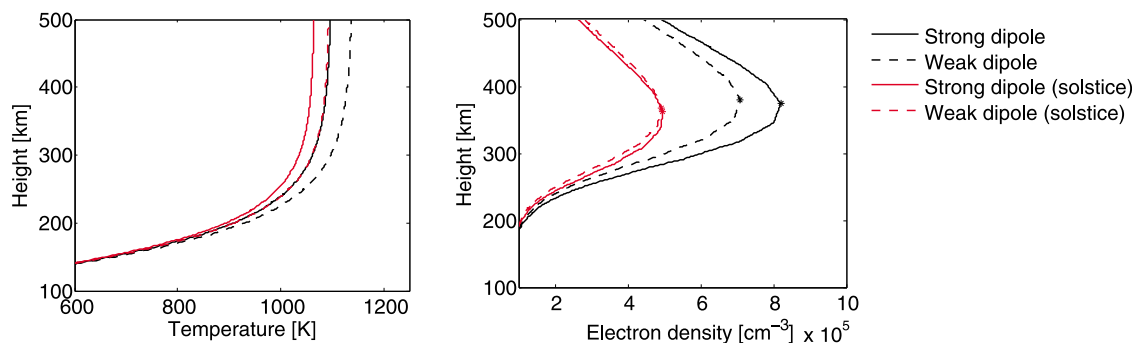


**Figure 6.** (left) Global mean temperature and (right) electron density profile for (solid line) the strong dipole and (dashed line) the weak dipole for (black) equinox and (red) solstice. The height of the peak electron density is marked with an asterisk.

**Table 7.** Global Mean Exospheric Temperature for the Strong Dipole, Weak Dipole, and the Difference (Weak-Strong Dipole): Mean and Standard Deviation Over the Last 24 h of the Simulations

Dipole	Exospheric Temperature (K)				
	March Equinox		June Solstice		
	Mean	$\sigma$	Mean	$\sigma$	
Strong dipole	1095	4	1062	6	
Weak dipole	1138	3	1090	4	
Weak-strong	42	2	28	2	

upwards, as they tend to stay on constant-pressure surfaces. This is confirmed by the global mean electron density profiles for the strong and weak dipoles, shown in Figure 6 (right). At equinox, the electron density is also strongly affected, while there is little difference at solstice. The mean changes in the peak electron density and the height of the peak electron density are given in Table 8.

[35] As for the response in temperature, the ionospheric responses are not spatially uniform, and the global mean presents an oversimplified picture. Figure 7 (top) therefore shows the spatial structure of the height of the peak of the F2 layer, hmF2, for the strong dipole and the difference (weak-strong dipole) averaged from 13 to 15 UT for equinox conditions. Some regions show a strong increase in hmF2, e.g., over the northern Pacific Ocean (20°N–60°N; 140°E–160°W and 0°N–30°N; 140°E–90°W), the southeastern Pacific Ocean (0–60°S; 100°W–40°W), and southeast Australia (0–60°S; 120°E–180°E), while a few others show a decrease, e.g., over North America (40°N–70°N; 160°W–80°W), the Caribbean (20°N–40°N; 90°W–60°W), the central southern Pacific Ocean (30°S–60°S; 180°W–140°W), and the Indian Ocean and eastern Africa (5°S–20°N; 20°E–120°E). These features move with local time.

[36] Some of the changes in hmF2 are related to changes in the neutral winds, which drag ions up and down magnetic field lines. The vertical component of the horizontal neutral wind parallel to the magnetic field,  $v_{n,par,v}$  [see *Cnossen and Richmond*, 2008], which is responsible for this effect, is shown in Figure 7 (middle). A positive change in  $v_{n,par,v}$  indicates an uplifting effect on hmF2, and vice versa. The increase in hmF2 over the North Pacific and partly also the decrease over the South Pacific are due to a relative enhancement of southward winds that push ions and electrons up magnetic field lines toward the magnetic equator in the NH, corresponding to a positive change in  $v_{n,par,v}$ , and down magnetic field lines away from the magnetic equator in the SH, corresponding to a negative change in  $v_{n,par,v}$ . The strong increase in hmF2 over southeast Australia is also related to an enhancement in  $v_{n,par,v}$ .

[37] Other changes are due to changes in the vertical  $\mathbf{E} \times \mathbf{B}$  drift, shown in Figure 7 (bottom). Changes in the vertical component of the  $\mathbf{E} \times \mathbf{B}$  drift are most effective at low magnetic latitudes, where the plasma will not easily diffuse back up or down because the magnetic field lines are nearly horizontal. The relatively small negative enhancement over the Indian Ocean could therefore be responsible for the decrease in hmF2 there, even though some of the much larger changes in the vertical  $\mathbf{E} \times \mathbf{B}$  drift occurring at high

magnetic latitudes seem to have little effect. Nevertheless, the negative changes in the  $\mathbf{E} \times \mathbf{B}$  drift over western Canada and the South Pacific do appear to have contributed to a decrease in hmF2 over those regions, even though they are at midlatitudes and high latitudes.

[38] Figure 8 (top) shows the spatial structure of the critical frequency of the F2 layer, foF2, which is proportional to the square root of the peak electron density, for the strong dipole and the difference (weak-strong dipole) averaged from 13 to 15 UT for equinox conditions. Figure 8 (bottom) shows the O/N<sub>2</sub> ratio at a fixed pressure level ( $3.2 \times 10^{-8}$  hPa), which gives an indication of the balance between ion production and loss processes. A larger O/N<sub>2</sub> ratio indicates that ion production is relatively more dominant, which leads to larger ion and electron densities. The close correspondence between the difference fields of foF2 and the O/N<sub>2</sub> ratio suggests that the differences in foF2 can be largely explained by changes in the O/N<sub>2</sub> ratio. The changes in the O/N<sub>2</sub> ratio themselves are likely to be due to changes in horizontal transport and changes in the neutral temperature structure. No substantial changes in vertical transport were found, except at high latitudes (not shown).

## 4. Discussion

### 4.1. Comparison With Previous Studies

[39] The theoretical scaling for the standoff distance  $R_s$  with  $M$  ( $R_s \propto M^{1/3}$ ) would predict a ratio between the strong and weak dipole  $R_s$  of  $(8/6)^{1/3} = 1.1$ . If we consider the  $R_s$  for the strong dipole as the reference value, this scaling relation would predict the  $R_s$  values for the weak dipole as 9.0  $R_E$  (equinox) and 9.4  $R_E$  (solstice). Our modeled values are slightly lower than this (see Table 1), indicating a slightly stronger dependence of  $R_s$  on  $M$ . While this is in agreement with the modification to the standard theoretical scaling as suggested by *Zieger et al.* [2006b], the differences are small and may be within the error margin of the model. Also in agreement with *Zieger et al.* [2006b], we confirmed that the magnetosphere retains its shape for different values of  $M$  and thus behaves in a self-similar way, at least on the dayside.

[40] *Siscoe and Chen* [1975] derived a theoretical scaling relation for the polar cap by equating the magnetic flux through the tail of the magnetosphere to the magnetic flux through the polar cap. They found that  $\cos \lambda_{pc} \propto M^{-1/6}$ , where  $\lambda_{pc}$  is the latitude of the boundary of the polar cap. *Zieger et al.* [2006b] found a slightly stronger dependence of

**Table 8.** Global Mean Maximum Electron Density and the Height of the Global Mean Electron Density Maximum for the Strong Dipole, Weak Dipole, and the Difference (Weak-Strong Dipole): Mean and Standard Deviation Over the Last 24 h of the Simulations

Dipole	Max. Electron Density ( $10^5 \text{ cm}^{-3}$ )				Max. Electron Density Height (km)			
	March Equinox		June Solstice		March Equinox		June Solstice	
	Mean	$\sigma$	Mean	$\sigma$	Mean	$\sigma$	Mean	$\sigma$
Strong dipole	8.2	0.2	4.8	0.3	373	1	362	1
Weak dipole	7.2	0.1	4.7	0.2	379	1	366	<1
Weak-strong	-1.0	0.06	-0.05	0.15	6	1	4	1

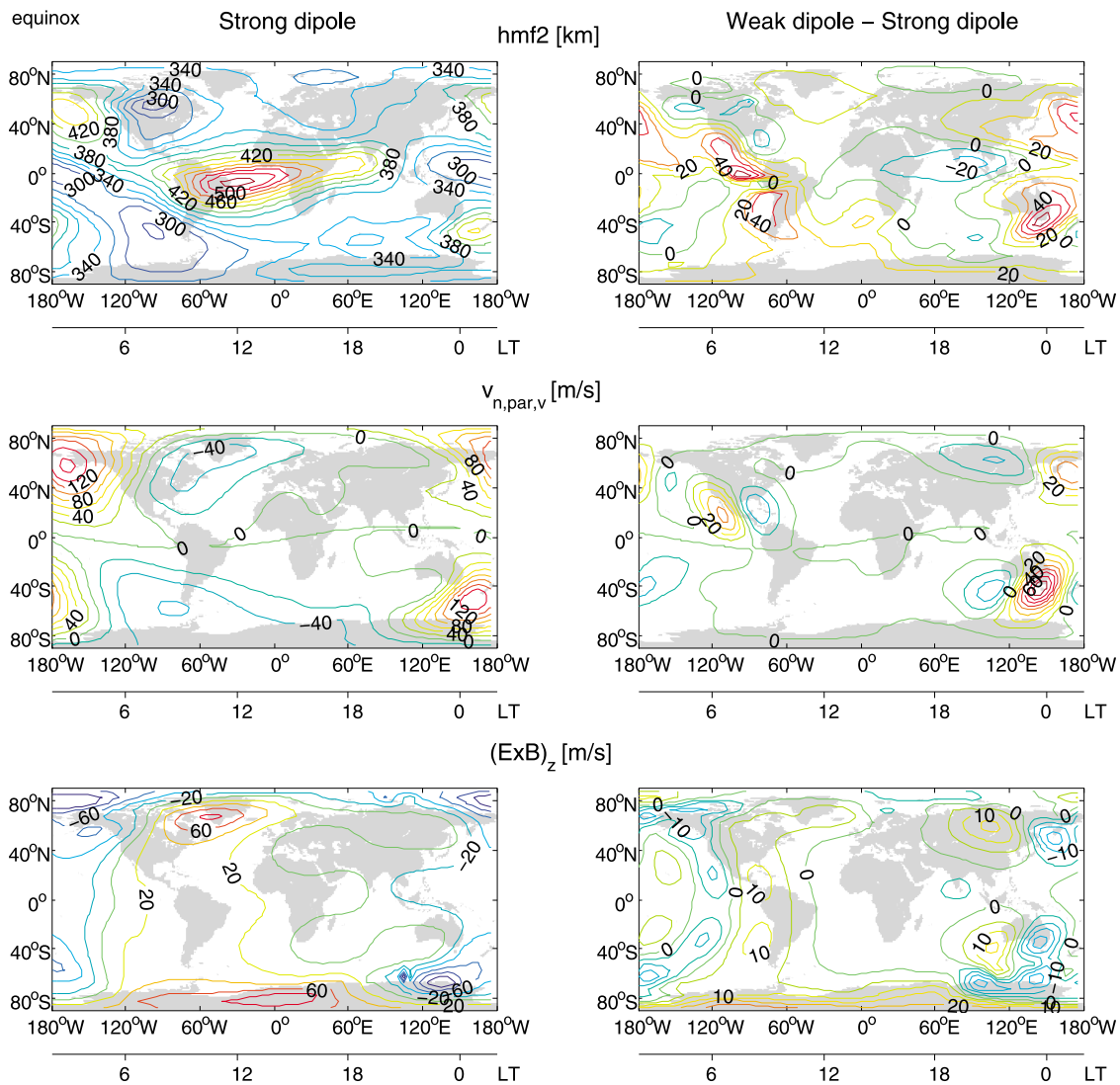


**Figure 7.** The height of the peak of the F2 layer, (top) hmf2, (middle) the vertical component of the neutral wind parallel to the Earth's magnetic field,  $v_{n,\text{par},v}$ , at  $3.2 \times 10^{-8}$  hPa, and (bottom) the vertical component of the  $\mathbf{E} \times \mathbf{B}$  drift at  $3.2 \times 10^{-8}$  hPa for (left) the strong dipole and (right) the weak-strong dipole for equinox at 13–15 UT in geographic coordinates.

$\cos \lambda_{\text{pc}}$  on  $M$ , which suggested the exponent should be approximately  $-0.19$  instead of  $-1/6$  ( $\approx -0.17$ ). Our results suggest a very similar dependence for equinox, for which we predict an exponent of  $-0.17$ , but a stronger dependence for solstice, with an exponent of  $-0.24$ . Similarly, our results suggest a slightly stronger change in the polar cap area than would be expected from self-similarity. The area of the polar cap is approximately proportional to the square of the colatitude of the polar cap boundary,  $\theta_{\text{pc}}$ , or to the inverse of the  $L$  value of this boundary. If the magnetosphere is self-similar, the boundary  $L$  value should scale with  $M$  in the same way as the standoff distance, so that

$$\text{area}_{\text{pc}} \propto \theta_{\text{pc}}^2 \propto \frac{1}{L} \propto M^{-1/3}. \quad (5)$$

[41] This gives an expected increase in the polar cap area of  $\sim 10\%$ , compared with the 11%–14% change we

simulated. However, a difference of a few percent in the polar cap area or a few tenths of degrees in the polar cap latitude can already make these kinds of differences. Given the standard deviations on the polar cap area and latitude, this means that our results are not significantly different from the estimates of *Siscoe and Chen* [1975] and *Zieger et al.* [2006b] and the assumption of self-similarity.

[42] *Zieger et al.* [2006a] investigated the dependence of the cross-polar cap potential and region 1 field-aligned currents with BATS-R-US and the analytical Hill model. For the same reduction in dipole strength and the same IMF conditions as used here, their BATS-R-US simulations gave an  $\sim 30\%$  reduction in cross-polar cap potential and an  $\sim 5\%$  reduction in field-aligned currents, while the Hill model predicted a  $\sim 15\%$  reduction in cross-polar cap potential and an  $\sim 13\%$  increase in field-aligned currents. Somewhat surprisingly, the latter are in fact in best agreement with our results.

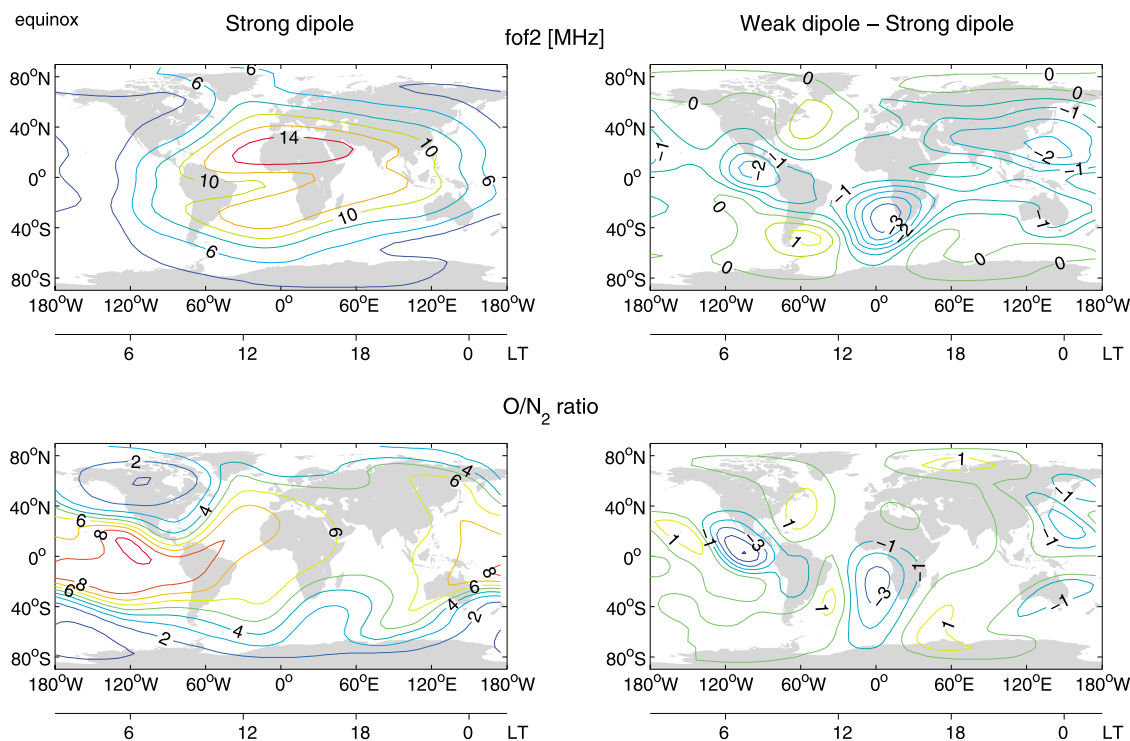


**Figure 8.** The F2 layer critical frequency, (top) foF2, and (bottom) the O/N<sub>2</sub> ratio at  $3.2 \times 10^{-8}$  hPa for (left) the strong dipole and (right) the weak-strong dipole for equinox at 13–15 UT in geographic coordinates.

[43] It must be noted that both estimates by Zieger *et al.* [2006a] as well as the studies by Glassmeier *et al.* [2004] and Zieger *et al.* [2006b] assumed that  $\Sigma_P \propto M^{-1}$ . This is in contradiction with an empirical relationship given by Richmond [1995], from which it follows that  $\Sigma_P \propto M^{-1.6}$  and  $\Sigma_H \propto M^{-1.3}$ . Our simulated changes in the Pedersen and Hall conductances suggest coefficients of approximately  $-1.5$  and  $-1.7$ , respectively, for their dependence on  $M$ . Our results for the Pedersen conductance thus agree very well with those of Richmond [1995], while the dependency used by Glassmeier *et al.* [2004] and Zieger *et al.* [2006a, 2006b] seems too weak. Our result for the Hall conductance implies a somewhat stronger dependence on  $M$  than suggested by Richmond [1995]. It should be noted that these dependencies are valid only for the dayside. On the nightside, the dependence of the Hall and Pedersen conductance on  $M$  is weaker.

#### 4.2. CMIT Versus TIE-GCM

[44] In the introduction, it was argued that the magnetosphere, thermosphere, and ionosphere should be studied as a coupled system to capture the full response of each individual component, as well as the system as a whole, to a change in magnetic field strength. We have tested if this is indeed the case by comparing the results from the coupled simulations with results obtained from the stand-alone TIE-GCM.

[45] The stand-alone TIE-GCM was run for a period of 20 days under equinox conditions, with a cross-polar cap potential of 120 kV specified by the Heelis *et al.* [1982] model, and a hemispheric power of precipitating particles of 6 GW. These values are similar to the ones obtained from the CMIT simulations, but for the TIE-GCM simulations

they are kept the same for the strong and the weak dipole cases. The last 24 h of the TIE-GCM simulations are used to compare with the last 24 h of the CMIT simulations for equinox.

[46] Table 9 gives the mean exospheric temperature and mean hmF2 and their standard deviations for the TIE-GCM strong and weak dipole simulations. The differences are larger than for the CMIT simulations (compare with Tables 7 and 8). This may be due to the fact that the high-latitude electric potential was fixed in the TIE-GCM simulations, resulting in a larger change in  $\mathbf{E} \times \mathbf{B}$  drifts (scaling as  $E/B$ ), and therefore a larger change in Joule heating.

[47] This is important only when the high-latitude electric potential is relatively strong. TIE-GCM simulations carried out with a much lower cross-polar cap potential of 20 kV showed nearly no difference between the strong and weak

**Table 9.** Global Mean Exospheric Temperature and the Height of the Global Mean Electron Density Maximum for the Strong Dipole, Weak Dipole, and the Difference (Weak-Strong Dipole): Mean and Standard Deviation Over the Last 24 h of the Simulations With the Stand-Alone TIE-GCM for March Equinox

Stand-Alone TIE-GCM Dipole	March Equinox			
	Exospheric Temperature (K)		Max. Electron Density Height (km)	
	Mean	$\sigma$	Mean	$\sigma$
Strong dipole	1087	1	372	1
Weak dipole	1145	1	368	1
Weak-strong	58	1	4	1

dipoles. The CMIT response to a change in magnetic field strength would also be expected to be smaller under weaker magnetospheric driving conditions.

#### 4.3. Implications for Long-Term Trend Studies

[48] We have shown that a 25% reduction in magnetic field strength has a substantial effect on the thermosphere-ionosphere system. Changes in field strength in the recent historic past have been considerably smaller, at an  $\sim 5\%$  decrease per century since 1840. While it is not the aim of the present study to compare directly with observed trends, we can give a rough estimate of the contribution of the decrease in magnetic field strength over the past century to changes in the thermosphere-ionosphere system.

[49] If we assume a linear response, a 5% decrease in magnetic field strength could cause an increase of 8–9 K in the global mean exospheric temperature during equinox and local changes in hmF2 of up to  $\pm 5$ –10 km. Observed long-term trends in hmF2, extrapolated to a period of 100 years, would imply changes in hmF2 of the order of  $\pm 20$ –40 km (depending strongly on the station) [see, e.g., *Cnossen and Richmond*, 2008]. As a rough estimate, changes in magnetic field intensity could thus be responsible for  $\sim 25\%$  of observed trends, although this will vary strongly with location. In future work we will perform simulations with historic magnetic fields to quantify more precisely the effect of changes in the magnetic field on the magnetosphere-ionosphere-thermosphere system for comparison with observed trends.

#### 5. Summary and Conclusions

[50] We simulated the effect of a 25% reduction of the dipole moment of the Earth's internal magnetic field on the coupled magnetosphere-ionosphere-thermosphere system, using the CMIT model. Our main findings are as follows.

[51] 1. The standoff distance was reduced by 1.1  $R_E$ , in agreement with theoretical predictions.

[52] 2. The shape of the magnetosphere did not significantly change.

[53] 3. The area of the polar cap expanded by 11%–14%, and its low-latitude boundary moved equatorward by  $\sim 1^\circ$ .

[54] 4. The ionospheric conductivity increased by 50%–60% (Pedersen) and 60%–65% (Hall) on the dayside, with smaller changes on the nightside.

[55] 5. The high-latitude electric potential decreased by  $\sim 9\%$ –12%, and field-aligned currents were enhanced by  $\sim 0\%$ –30% (depending on the season).

[56] 6. Ion  $\mathbf{E} \times \mathbf{B}$  drift velocities were enhanced by  $\sim 10\%$ –15%.

[57] 7. The combined changes in ionospheric Pedersen conductivity, magnetic field strength, ion  $\mathbf{E} \times \mathbf{B}$  drifts, and neutral winds caused an increase in high-latitude Joule heating of 16%–30%, depending on the season.

[58] 8. The increase in  $\mathbf{E} \times \mathbf{B}$  drifts caused a strengthening of the neutral wind at high latitudes.

[59] 9. At low latitudes and midlatitudes, changes in neutral temperature and neutral wind formed together.

[60] 10. The changes in the neutral wind, together with enhancements in the vertical  $\mathbf{E} \times \mathbf{B}$  drift, caused globally nonuniform changes in hmF2 of up to  $-40$  and  $+60$  km.

[61] 11. An overall reduction in peak electron density for equinox conditions was largely due to a reduction in the  $O/N_2$  ratio.

[62] 12. Responses were larger for the stand-alone TIE-GCM, without the high-latitude coupling to the magnetosphere.

[63] **Acknowledgments.** We thank Asher Pembroke for sharing code that was used for some of the data analysis in this paper. Parts of this work were supported by NASA LWS grant NNH07AF041 and parts were supported by the Center for Integrated Space Weather Modeling (CISM), which is funded by the STC Program of the National Science Foundation under agreement ATM-0120950, NASA grant NNX06AC40G, and National Natural Science Foundation of China grant 40621003. The National Center for Atmospheric Research is sponsored by the National Science Foundation.

[64] Robert Lysak thanks the reviewers for their assistance in evaluating this paper.

#### References

- Cnossen, I., and A. D. Richmond (2008), Modelling the effects of changes in the Earth's magnetic field from 1957 to 1997 on the ionospheric hmF2 and foF2 parameters, *J. Atmos. Sol. Terr. Phys.*, *70*(11–12), 1512–1524, doi:10.1016/j.jastp.2008.05.003.
- Finlay, C. C., et al. (2010), International Geomagnetic Reference Field: The eleventh generation, *Geophys. J. Int.*, *183*, 1216–1230, doi:10.1111/j.1365-246X.2010.04804.x.
- Glassmeier, K.-H., J. Vogt, A. Stadelmann, and S. Buchert (2004), Concerning long-term geomagnetic variations and space climatology, *Ann. Geophys.*, *22*(10), 3669–3677, doi:10.5194/angeo-22-3669-2004.
- Gubbins, D., A. L. Jones, and C. C. Finlay (2006), Fall in Earth's magnetic field is erratic, *Science*, *312*(5775), 900–902, doi:10.1126/science.1124855.
- Guyodo, Y., and J.-P. Valet (1999), Global changes in intensity of the Earth's magnetic field during the past 800 kyr, *Nature*, *399*(6733), 249–252, doi:10.1038/20420.
- Heelis, R. A., J. K. Lowell, and R. W. Spiro (1982), A model of the high-latitude ionospheric convection pattern, *J. Geophys. Res.*, *87*(A8), 6339–6345, doi:10.1029/JA087iA08p06339.
- Hill, T. W., A. J. Dessler, and R. A. Wolf (1976), Mercury and Mars: The role of ionospheric conductivity in the acceleration of magnetospheric particles, *Geophys. Res. Lett.*, *3*(8), 429–432, doi:10.1029/GL003i008p00429.
- Kivelson, M. G., and C. T. Russell (1995), *Introduction to Space Physics*, 568 pp., Cambridge Univ. Press, New York.
- Korth, H., B. J. Anderson, M. J. Wiltberger, G. Lyon, and P. C. Anderson (2004), Intercomparison of ionospheric electrodynamic from the Iridium constellation with global MHD simulations, *J. Geophys. Res.*, *109*, A07307, doi:10.1029/2004JA010428.
- Lyon, J. G., J. A. Fedder, and C. M. Mobarry (2004), The Lyon-Fedder-Mobarry (LFM) global MHD magnetospheric simulation code, *J. Atmos. Sol. Terr. Phys.*, *66*(15–16), 1333–1350, doi:10.1016/j.jastp.2004.03.020.
- Richmond, A. D. (1995), Ionospheric electrodynamic, in *Handbook of Ionospheric Electrodynamics*, vol. 2, pp. 249–290, CRC Press, Boca Raton, Fla.
- Richmond, A. D., E. C. Ridley, and R. G. Roble (1992), A thermosphere/ionosphere general circulation model with coupled electrodynamic, *Geophys. Res. Lett.*, *19*(6), 601–604, doi:10.1029/92GL00401.
- Roble, R. G., E. C. Ridley, A. D. Richmond, and R. E. Dickinson (1988), A coupled thermosphere/ionosphere general circulation model, *Geophys. Res. Lett.*, *15*(12), 1325–1328, doi:10.1029/GL015i012p01325.
- Siscoe, G. L., and C.-K. Chen (1975), The paleomagnetosphere, *J. Geophys. Res.*, *80*(34), 4675–4680, doi:10.1029/JA080i034p04675.
- Siscoe, G. L., G. M. Erickson, B. U. O. Sonnerup, N. C. Maynard, J. A. Schoendorf, K. D. Siebert, D. R. Weimer, W. W. White, and G. R. Wilson (2002a), Hill model of transpolar potential saturation: Comparisons with MHD simulations, *J. Geophys. Res.*, *107*(A6), 1075, doi:10.1029/2001JA000109.
- Siscoe, G. L., N. U. Crooker, and K. D. Siebert (2002b), Transpolar potential saturation: Roles of region 1 current system and solar wind ram pressure, *J. Geophys. Res.*, *107*(A10), 1321, doi:10.1029/2001JA009176.
- Wang, W., M. Wiltberger, A. G. Burns, S. C. Solomon, T. L. Killeen, N. Maruyama, and J. G. Lyon (2004), Initial results from the coupled magnetosphere-ionosphere-thermosphere model: Thermosphere-ionosphere responses, *J. Atmos. Sol. Terr. Phys.*, *66*(15–16), 1425–1441, doi:10.1016/j.jastp.2004.04.008.
- Wang, W. B., J. H. Lei, A. G. Burns, M. Wiltberger, A. D. Richmond, S. C. Solomon, T. L. Killeen, E. R. Talaat, and D. N. Anderson (2008),

- Ionospheric electric field variations during a geomagnetic storm simulated by a coupled magnetosphere ionosphere thermosphere (CMIT) model, *Geophys. Res. Lett.*, *35*, L18105, doi:10.1029/2008GL035155.
- Weimer, D. R. (1995), Models of high-latitude electric potentials derived with a least error fit of spherical harmonic coefficients, *J. Geophys. Res.*, *100*(A10), 19,595–19,607, doi:10.1029/95JA01755.
- Weimer, D. R. (2005), Predicting surface geomagnetic variations using ionospheric electrodynamic models, *J. Geophys. Res.*, *110*, A12307, doi:10.1029/2005JA011270.
- Wiltberger, M., W. Wang, A. G. Burns, S. C. Solomon, J. G. Lyon, and C. C. Goodrich (2004), Initial results from the coupled magnetosphere ionosphere thermosphere model: Magnetospheric and ionospheric responses, *J. Atmos. Sol. Terr. Phys.*, *66*(15–16), 1411–1423, doi:10.1016/j.jastp.2004.03.026.
- Wiltberger, M., R. S. Weigel, W. Lotko, and J. A. Fedder (2009), Modeling seasonal variations of auroral particle precipitation in a global-scale magnetosphere-ionosphere simulation, *J. Geophys. Res.*, *114*, A01204, doi:10.1029/2008JA013108.
- Zieger, B., J. Vogt, A. J. Ridley, and K. H. Glassmeier (2006a), A parametric study of magnetosphere-ionosphere coupling in the paleomagnetosphere, *Adv. Space Res.*, *38*, 1707–1712, doi:10.1016/j.asr.2005.04.077.
- Zieger, B., J. Vogt, and K.-H. Glassmeier (2006b), Scaling relations in the paleomagnetosphere derived from MHD simulations, *J. Geophys. Res.*, *111*, A06203, doi:10.1029/2005JA011531.
- 
- I. Cnossen, A. D. Richmond, P. Schmitt, W. Wang, and M. Wiltberger, High Altitude Observatory, National Center for Atmospheric Research, Boulder, CO 80301, USA. (icnossen@ucar.edu)